IEEE Access
Multidisciplinary | Rapid Review | Open Access Journal

Received January 3, 2020, accepted February 3, 2020, date of publication February 6, 2020, date of current version February 13, 2020.

Digital Object Identifier 10.1109/ACCESS.2020.2972017

Multiphysics Analysis of an Axial-Flux In-Wheel Motor With an Amorphous Alloy Stator

TAO LI, YOUTONG ZHANG, YUXIU LIANG, QIANG AI, AND HAISHI DOU
Laboratory of Low Emission Vehicle, Beijing Institute of Technology, Beijing 100081, China
Corresponding author: Youtong Zhang (youtong@bit.edu.cn)

ABSTRACT This paper presents a novel yokeless and segmented armature (YASA) axial-flux in-wheel motor with amorphous magnetic material (AMM) stator cores for a solar-powered electric vehicle. Although this new axial-flux in-wheel motor has many advantages such as high efficiency, shorter axial length, and high power density, its working condition is complicated. In-wheel motors are usually operated in electromagnetic, thermal, and other multiphysics environments. Increasing the performance requirements of in-wheel motors, such as power density, efficiency, and reliability, requires a multiphysics design approach. The focus of this paper is on the analysis of electromagnetic characteristics, losses, temperature distribution, mechanical behavior and other characteristics of the axial-flux in-wheel motor. The back electromotive force (EMF) and electromagnetic torque of the motor with harmonic current are obtained by the 3-D finite element method (FEM). The permanent magnet (PM) eddy-current losses when using different PM shapes are studied. The equivalent thermal model of the tape-wound AMM stator segments and the windings are established, and the temperature distribution of the motor is obtained. The mechanical behavior of the stator segments and the rotor disks when the motor is eccentric and axially offset is analyzed, and the structural strength of the motor is evaluated. Finally, a prototype of the motor is fabricated, and the electromagnetic performance and temperature of the motor are tested to verify the accuracy of the multiphysics design approach.

INDEX TERMS Amorphous alloy materials, axial-flux motors, in-wheel motors, permanent magnet motors, thermal analysis.

I. INTRODUCTION

During the past decades, much attention has been paid to the development of electric vehicles (EVs) and hybrid electric vehicles (HEVs) in the automobile industry [1], [2]. The EVs driven by in-wheel motors feature a promising structure because of the convenience of energy conversion and the reduction of mechanical losses [3], [4]. On the other side, the additional motor mass inside the wheel increases the unsprung mass of EVs, so a high power density motor is needed. Meanwhile, the space inside the wheel is strongly limited, so the in-wheel motor has to be axially short [5]. Axial-flux permanent magnet (PM) (AFPM) in-wheel motors have many distinguished advantages, such as high power/torque density, high efficiency, and compact axial length, and they are widely used in EVs [6]–[8]. The yokeless and segmented armature (YASA) topology is a new type of AFPM machine that comprises two external rotors and an inner stator [9], [10]. The stator yoke of the YASA machine is eliminated, and the stator segments are connected by lightweight material. Compared with other topologies of AFPM machines, the YASA has the advantages of short end-windings, convenient assembly, light stator weight, low iron and copper losses, and high fault tolerance. It is one of the promising topologies used for AFPM machines in recent years.

Amorphous magnetic metal (AMM) is a new type of soft magnetic material with the advantages of high permeability, low hysteresis losses, and low eddy-current losses [11]. Compared with the stator made of soft magnetic composite (SMC) or silicon steel, the motor with AMM has lower iron losses at high frequency [12]. Winding the amorphous alloy ribbon into a ring shape and slotting by a wire cutting process is a conventional stator manufacturing process [13]–[15]. However, the wire cutting process increases the iron loss coefficient of the AMM stator. A slotless AMM stator is also commonly used in AFPM machines that wrap the coil directly around the well-wound AMM cores. This structure can eliminate cogging torque and reduce noise [16]. However, the length of the air gap of the

The associate editor coordinating the review of this manuscript and approving it for publication was Shihong Ding.

slotless motor is increased, and it is necessary to improve the air gap flux density by increasing the thickness of the PM, thereby increasing the cost of the motor. In addition, placing the coil in the air gap also increases copper losses. To design the motor as a YASA topology, it is feasible to wrap the AMM ribbon into stator segments [17]. Compared with other AMM cores, the tape-wound AMM stator segments have the advantages of simple manufacturing, lightweight, and low iron losses. However, tape-wound segments are generally hollow, and there is less research on the electromagnetic properties of this type of stator.

The working environment of the in-wheel motor is quite harsh, so the requirements for sealing performance are stricter. This makes it difficult for the air to flow inside the motor. The temperature rise causes thermal deformation of each component, resulting in the sealing failure of the motor. Compared with the silicon steel stator core, the tape-wound AMM segment has a low thermal conductivity and laminated coefficient. Therefore, it is difficult for the heat generated by the AMM segment to be transferred to the surface of the stator support. This results in a high local temperature in the motor, which produces a hidden danger in the windings and PMs. Many scholars have designed an in-wheel motor to reduce electromagnetic losses and improve cooling performance [18]–[21]. The motor has different cooling modes depending on the operating fluid: liquid-cooled [22], [23], oil-cooled [24], [25], and air-cooled [26]. The air-cooled mode has the advantages of a simple cooling system configuration. However, its cooling capacity is relatively small. Therefore, it is necessary to achieve high accuracy in the equivalent thermal model of the tape-wound AMM segment and obtain the temperature rise of each component to ensure the reliable operation of the in-wheel motor.

The precise calculation of the axial electromagnetic force is important to the structural design and guaranteed reliability of the motor [27]. To prevent the deformation of the rotor disk caused by the rotor-stator attraction force, a high-strength PM support is required. Due to the small contact area between the rotor disk and the bearing of the AFPM, defects such as motor shaft deformation, rotor mass imbalance, and assembly error easily cause eccentricity and axial offset defects. Additionally, these defects will cause axial unbalanced magnetic force (UMF), torque ripple and noise, which will aggravate the wear of the winding insulation and the bearing, and the performance and reliability of the motor will deteriorate [28]–[30]. When the eccentricity or axial offset is further aggravated, the rotor will scrape against the stator and damage the motor. The research on the change in electromagnetic characteristics [31] and fault detection method [32], [33] when the motor is eccentric or axially offset has received extensive attention. However, the AMM stator segments are independent of each other and the influence of electromagnetic force on a single stator segment is rarely studied when eccentricity or axial offset occurs. Moreover, the distribution characteristics of electromagnetic force should be taken into account in the calculation of the rotor bending moment when eccentricity defects occur. Otherwise, the results will be inaccurate [34]. Therefore, the motor strength problem should attract extensive attention and research.

In this paper, a novel YASA in-wheel motor with tape-wound AMM segments for a solar-powered electric vehicle is proposed. During the design process, a multiphysics analysis including electromagnetic, thermal, and mechanical behavior is indispensable [35]–[38]. This paper describes the design, the study and the construction of the prototype of the YASA in-wheel motor with 24 poles and 27slots. Moreover, the multiphysics modeling and analysis are described. The findings are proved with measurements on the 1.3kW, 560r/min prototype.

This paper is organized as follows. The description of the novel YASA in-wheel motor with AMM stator segments is presented in Section II. Section III presents the electromagnetic and structural characteristics of the motor. The equivalent thermal conductivity model of the wound AMM stator segment and windings is established, and the distribution of motor temperature is obtained. Moreover, the mechanical behavior of the stator segment and the rotor disk is analyzed when the rotor is eccentric and axially offset and the structural strength of the motor is evaluated. In section IV, a prototype of the axial-flux in-wheel motor is built and tested, and experimental results are provided. The conclusions are summarized in Section V.

II. THE AXIAL-FLUX IN-WHEEL MOTOR

The structure of the axial-flux in-wheel motor is shown in Fig. 1. The stator segment is wound using AMM ribbon and has a hollow round shape in the cross section.

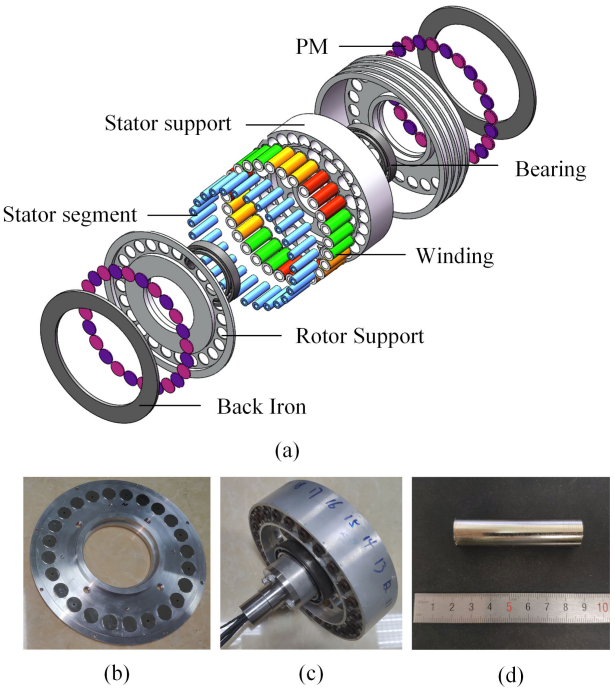

FIGURE 1. The axial-flux in-wheel motor. (a) Structural diagram, (b) Rotor, (c) Stator, (d) AMM segment.

An open-slot structure is used to avoid the influence of machining on the electromagnetic performance of the stator segment. Fractional-slot concentrated windings reduce the manufacturing and assembly costs considerably due to their shorter end-windings and prewound coils. The coils and stator segments are fixed by the stator support. The material of the PM is Nd-Fe-B N38UH, which is fixed to the rotor back iron and the rotor support to prevent it from moving at high speeds. Several cooling grooves are distributed on the outside of the rotor support to cool the motor by means of the incoming air when the vehicle is running. Both bearings are angular contact ball bearings 71918CA. The details of the winding coil distribution and the PMs are shown in Fig. 2. The upper and lower case letters mean that the coil windings are wound clockwise and counterclockwise, respectively. The main parameters of the YASA machine are shown in Table 1.

Compared with the analytical method, 2-D finite element method (FEM) and quasi 3-D FEM, the 3-D FEM is time-consuming and requires a large memory capacity [39], [40]. However, the 3-D FEM is more accurate and can fully consider the curvature effect and edge effect of the YASA machine, which is suitable for multiphysics research. Therefore, a 3-D finite element model developed in ANSYS is used to study the prototype in this paper. The calculation flow chart of the multiphysics model is shown in Fig. 3.

III. MULTIPHYSICS ANALYSIS

A. ELECTROMAGNETIC

The AFPM machine is fed by a current-controlled voltage source inverter (VSI), and the variable voltage source is obtained by pulse-width modulation (PWM). The time harmonics appear in the output voltage of the VSI, which is affected by the switching frequency of the VSI and the modulation ratio. The phase current waveforms for the VSI PWM-fed machine that correspond to a carrier frequency of 10 kHz and their harmonic components obtained by the fast Fourier transform (FFT) are provided in Figs. 4 and 5, respectively.

When the rotor of the motor rotates, the relative position of the PMs and the stator segments changes, and the magnetic circuit and the flux density distribution inside the motor changes accordingly. Fig. 6 shows the magnetic lines of the motor at a certain time. The main flux travels axially through the stator segments, whereas the torque is generated by the radial direction windings. The remanent flux density of AMM is less than 1.5 T. Therefore, the parameter design of the cross section area of the stator segment should meet the requirements of flux density. Fig. 7 shows the magnetic density of the stator segment and the back iron, respectively. The flux density at the inner and outer edges of the stator

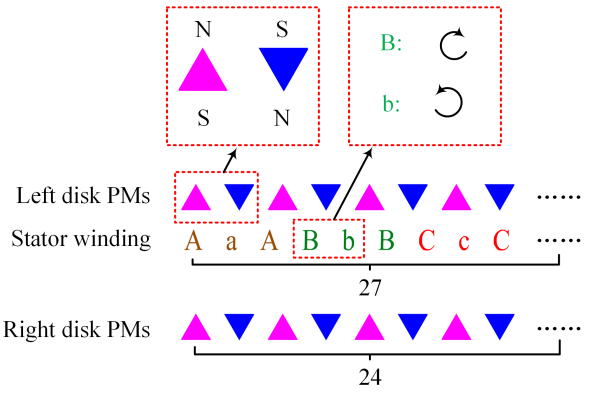

FIGURE 2. Schematic disposition of the coils (A, B, C, a, b, c) and the PMs (N, S).

TABLE 1. Main parameters of the AFPM motor.

Symbol	Description	Value
D_a	Active outer diameter	270 mm
D_i	Active inner diameter	202 mm
l_{ax}	Active axial length	86 mm
p	Number of pole pairs	12
N_s	Number of stator segments	27
g_0	Axial length of air gap	1 mm
l_s	Axial length of stator	64 mm
l_b	Axial length of rotor back iron	6 mm
l_m	Axial length of magnets	4 mm
N_{rated}	Rated rotational speed	560 r/min

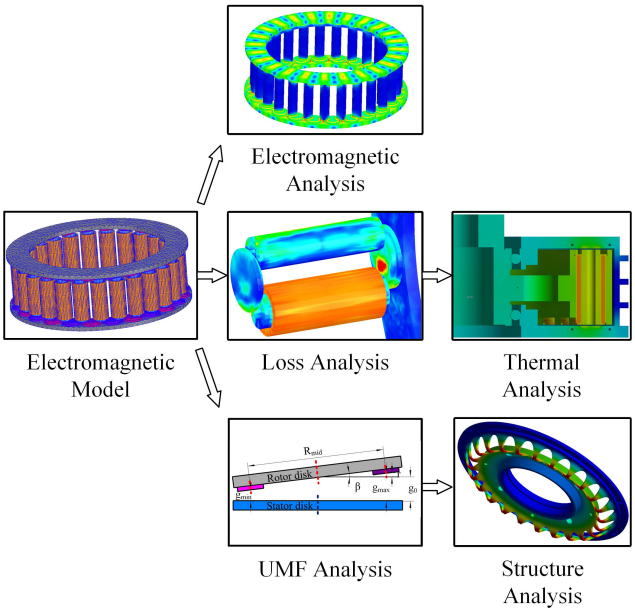

FIGURE 3. Calculation flow chart of the multiphysics model.

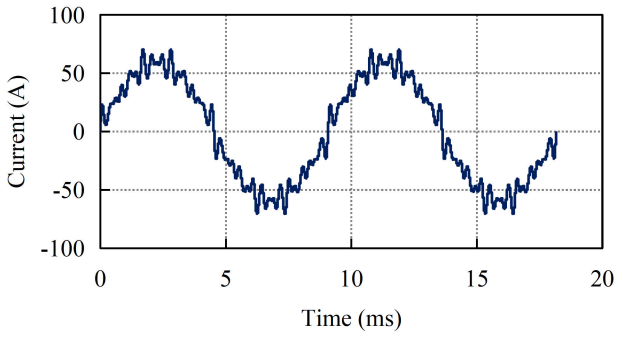

FIGURE 4. Current waveform.

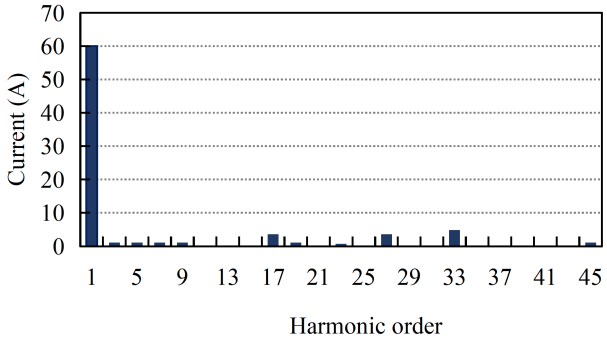

FIGURE 5. Current harmonic components.

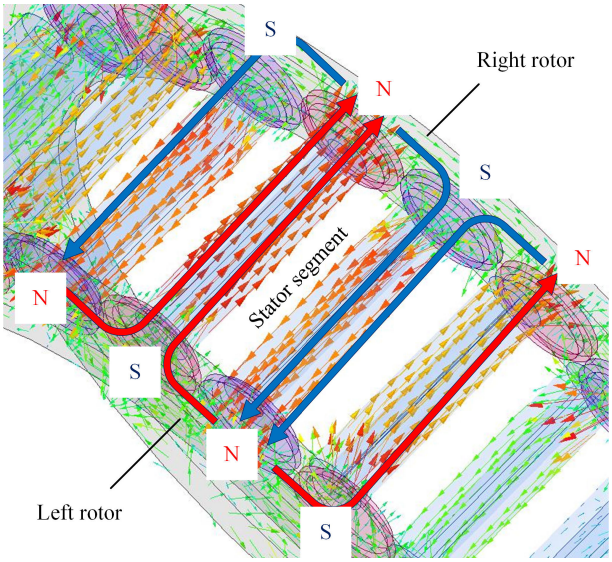

FIGURE 6. 3-D magnetic lines of the motor.

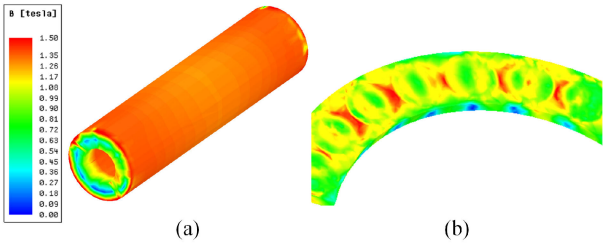

FIGURE 7. The flux density of (a) the stator segment and (b) the rotor back iron.

segment is large and slightly saturated, and the flux density in the segment is uniform. Flux leakage occurs between adjacent PMs, so the flux density between the PMs on the air gap side of the back iron is large.

Fig. 8 shows the three-phase no-load back electromotive force (EMF) at rated speed. The magnitude of each order harmonic of the back EMF of phase A is obtained by FFT, as shown in Fig. 9. The amplitude of the EMF fundamental wave is 27.6 V, and the third harmonic amplitude is the largest among the high-order EMF harmonics. The motor torque is shown in Fig. 10. The rated power of

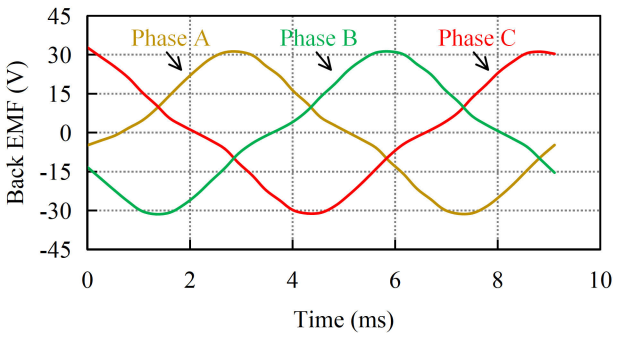

FIGURE 8. Back EMF.

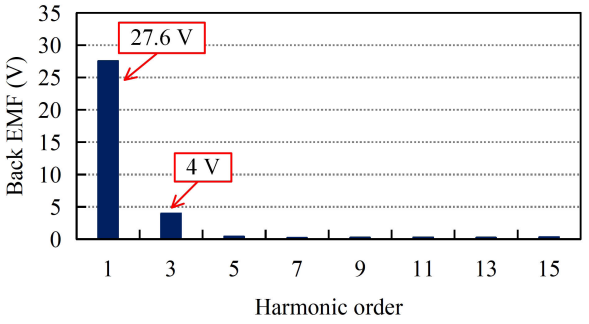

FIGURE 9. Harmonic components of the back EMF.

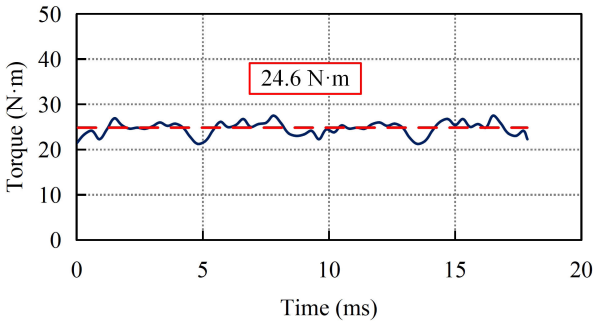

FIGURE 10. Electromagnetic torque.

the motor reaches 1.3 kW, which meets the requirements of solar-powered electric vehicles for the in-wheel motor.

B. THERMAL

The heat source of the motor is mainly electromagnetic losses. Coils, stator segments, back iron, and PMs are both heat-producing parts and heat conduction medium. The mathematical model of the total losses P_{total} of the motor is as follows [41], [42]:

$$P_{\text{total}} = P_{\text{Cu}} + P_{\text{Fe}} + P_{\text{Mag}} + P_{\text{Mec}} \tag{1}$$

$$P_{\text{Cu}} = 3I^2R \tag{2}$$

$$P_{\text{Fe}} = (K_{\text{h}} f B_{\text{m}}^{\alpha} + K_{\text{e}} \Delta_r^2 f^2 B_{\text{m}}^2 + K_{\text{exc}} f^{1.5} B_{\text{m}}^{1.5}) \cdot V_{\text{Fe}} \tag{3}$$

$$P_{\text{Mag}} = \int_{V_{\text{Mag}}} \frac{|J|^2}{\sigma_{\text{PM}}} dV_{\text{Mag}} \tag{4}$$

where P_{Cu} is the copper loss, P_{Fe} is the iron loss, P_{Mag} is the eddy-current loss of the PM, P_{Mec} is the mechanical loss,

I is the phase current of the winding, R is the DC resistance of single-phase winding, K_h is the hysteresis loss coefficient, K_e is the classical eddy-current loss coefficient, K_{exc} is the additional eddy-current loss coefficient, f is the alternating frequency, B_m is the flux density amplitude, Δ_r is the thickness of the AMM ribbon, and V_{Fe} is the stator core volume.

Due to the large ratio of the inner and outer diameters of the rotor, the proposed motor is suitable for round magnets. The eddy-current density loops and physical map of the round magnet are shown in Fig. 11(a) and (b), respectively. Conventional AFPM machines typically use fan-shaped unskewed magnets for which the eddy-current density is shown in Fig. 11(c). The fan-shaped unskewed PM has the advantages of simple design and convenient manufacture. However, the fan-shaped PM produces a larger cogging torque. PM skewing technology is usually used to reduce the cogging torque [43], such as dual skew magnets, classic skew magnets, and trapezoidal skew magnets. Their eddy-current density loops are shown in Fig. 11(d), (e), and (f), respectively. The distribution of eddy-current density loops with different skewing shape is slightly different. However, the eddy-current density at the corresponding position of the stator slot is the largest. Compared to other skew shapes, the round magnets and the rotor support matched with the round PMs are easier to the machine and reduce manufacturing costs.

The electromagnetic losses of each component of the motor are shown in Table 2.

AMM has hard and brittle physical properties, and the laminated coefficient is small. Therefore, heat is transferred mainly along the axial and circumferential direction, so it can be considered to be a multilayer flat-wall parallel heat conductor, as shown in Fig. 12. The axial and circumferential equivalent thermal conductivity λ_z and λ_φ can be expressed as:

$$\lambda_z = \lambda_\phi = \frac{\Delta_z \lambda_{Fe} + \delta_0 \lambda_0}{\Delta_z + \delta_0} = K_{Fe}\lambda_{Fe} + (1 - K_{Fe})\lambda 0 \qquad (5)$$

where Δ_z is the axial length of the stator, λ_{Fe} is the thermal conductivity of the AMM, δ_0 is the axial length of the insulation, λ_0 is the thermal conductivity of the insulation, and K_{Fe} is the laminated coefficient of the AMM.

The heat transfer along the radial direction can be considered to function as a multilayer plane-in-series heat conductor. The radial equivalent thermal conductivity λ_r can be expressed as:

$$\lambda_r = \frac{\Delta_r + \delta_0}{\frac{\Delta_r}{\lambda_{Fe}} + \frac{\delta_0}{\lambda_0}} = \frac{1}{\frac{K_{Fe}}{\lambda_{Fe}} + \frac{1 - K_{Fe}}{\lambda_0}} \qquad (6)$$

The distribution of the coils in the stator slot is complex. It is difficult to accurately model the insulation paint, insulating paper, copper wire paint film and air in the slot. To facilitate the calculation, the components in the stator slot are considered to be equivalent to copper on the inside and insulated material on the outside, as shown in Fig. 13. The total thermal resistance in the slot remains unchanged.

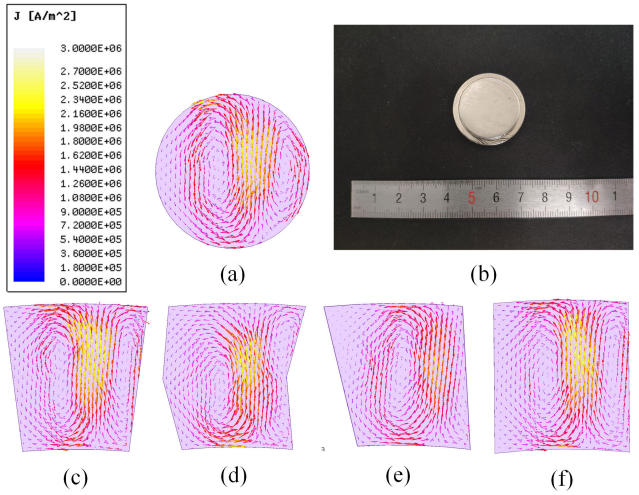

FIGURE 11. Eddy-current density loops of the PMs. (a) Round magnet, (b) Physical diagram of the round magnet, (c) Fan-shaped unskewed magnet, (d) Dual skew magnet, (e) Classic skew magnet, (f) Trapezoidal skew magnet.

TABLE 2. Losses of each component of the motor.

Components	Winding	Stator core	Rotor core	PM
Losses (W)	72.87	15.56	1.46	11.11

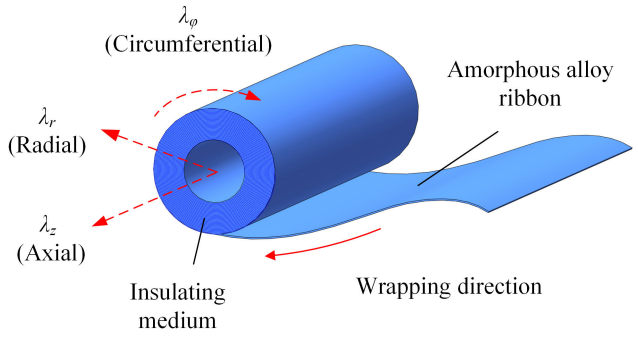

FIGURE 12. The wrapping process and the AMM core.

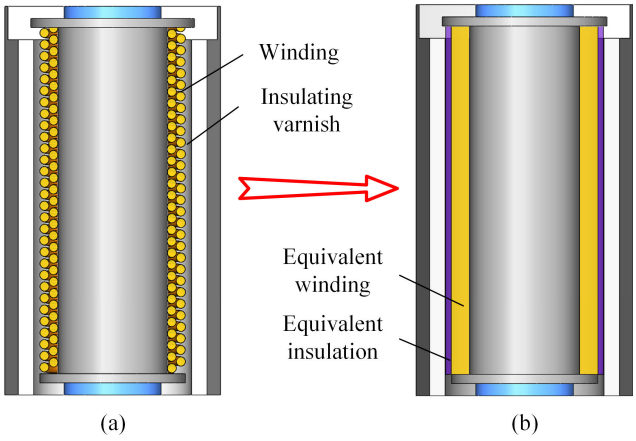

FIGURE 13. Equivalent model of the winding. (a) Initial model, (b) Equivalent model.

TABLE 3. Thermal conductivity of each part of the motor.

Components	Thermal conductivity/W/(m·°C)		
	Axial (z)	Circumferential (φ)	Radial (r)
Stator core	16.28	16.28	1.8
Rotor core	39	39	4.43
Winding	0.8	385	0.8
PM	9	9	9
Stator support	25.2	25.2	25.2
Air gap	0.0478	0.0478	0.0478
Equivalent insulation	0.12	0.12	0.12
Winding support	0.25	0.25	0.25
Air	0.026	0.026	0.026

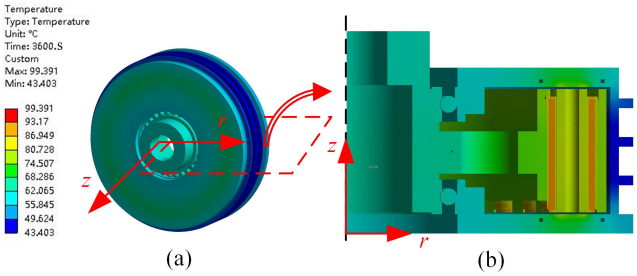

FIGURE 14. Temperature distribution of (a) the surface of the motor and (b) the axial section of the motor.

The thermal conductivity of the equivalent insulation λ_1 can be expressed as:

$$\lambda_1 = \frac{\sum_{i=1}^{n} \delta_i}{\sum_{i=1}^{n} \frac{\delta_i}{\lambda_i}} \tag{7}$$

where λ_i is the average thermal conductivity of each component in the stator slot and δ_i is the equivalent thickness of components in the stator slot.

The calculation method of the thermal conductivity of the other components is the same as that of the radial-flux motor, and the results are shown in Table 3.

The temperature of the environment is 25°C. The operating time of the motor is 3600 s, and the temperature of each component is stable. It can be seen from Fig. 14 that the temperature distribution of the motor decreases from the winding to the shaft end of the stator support and the rotor heat sink. The maximum temperature is 99.39°C, located at the stator winding. The minimum temperature is 43.4°C, located at the rotor heat sink. Windings are the highest-temperature heat source in the motor. The equivalent insulation and the winding support have a heat insulation effect, which causes the temperature difference between the windings and stator segments. Due to the higher thermal conductivity of the stator segment in the axial direction, the temperature difference between the middle part and the end part of the stator segment is small. The temperature of the air gap side of the PM is higher, and the other side is in contact with the back iron, which can be cooled by the airflow. Fig. 15 shows the temperature of each component. The temperature change of each component during the first 600 s is fast, and then it gradually stabilizes. Because of the heat insulation effect of the air gap, the temperatures of the windings and stator segments are similar, and the temperatures of the PMs and rotor support are similar.

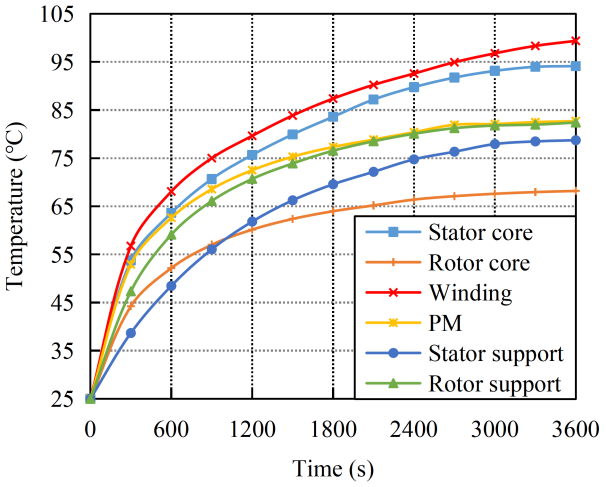

FIGURE 15. The temperature rise of each component.

C. MECHANICAL

Both the stator and rotor of the motor are subjected to the high axial electromagnetic force. Therefore, the strength of the connection mechanism of the stator segment and the rotor disk needs to meet the design requirements. Due to the eccentric and axial offset defects of the motor after running for a period of time, the stator segment and the rotor disk will also be subjected to axial UMF and bending moment. The motor has three centers in operation, including the stator center, rotor center, and rotor rotation center. In ideal cases, the three centers coincide, and the air gap is uniform, as shown in Fig. 16 (a). For the convenience of analysis, the stator and rotor disks are simplified, as shown in Fig. 16 (b). Eccentricity refers to the fact that the stator center, the rotor center and the rotor rotating center do not coincide and are generally ideal simplified into three cases: static eccentric (SE), dynamic eccentric (DE) and mixed eccentric (ME). In the case of SE, the rotor rotation center coincides with the rotor center but does not coincide with the stator center. When the rotor rotates, the position of the air gap is fixed with reference to the stator, as shown in Fig .16 (c). In the case of DE, the rotor rotation center coincides with the stator center but does not coincide with the rotor center. The air gap position rotates synchronously with the rotor, but the minimum and maximum values of the air gap length do not change, as shown in Fig. 16 (d), (e), and (f). In the case of ME, none of the rotor rotation center, stator center, or rotor center coincide, which is the linear superposition of static eccentricity and dynamic eccentricity. Rotor axial offset (AO) refers to the length of one-sided air gap or double-sided air gap deviation from the design value of the air gap, which can

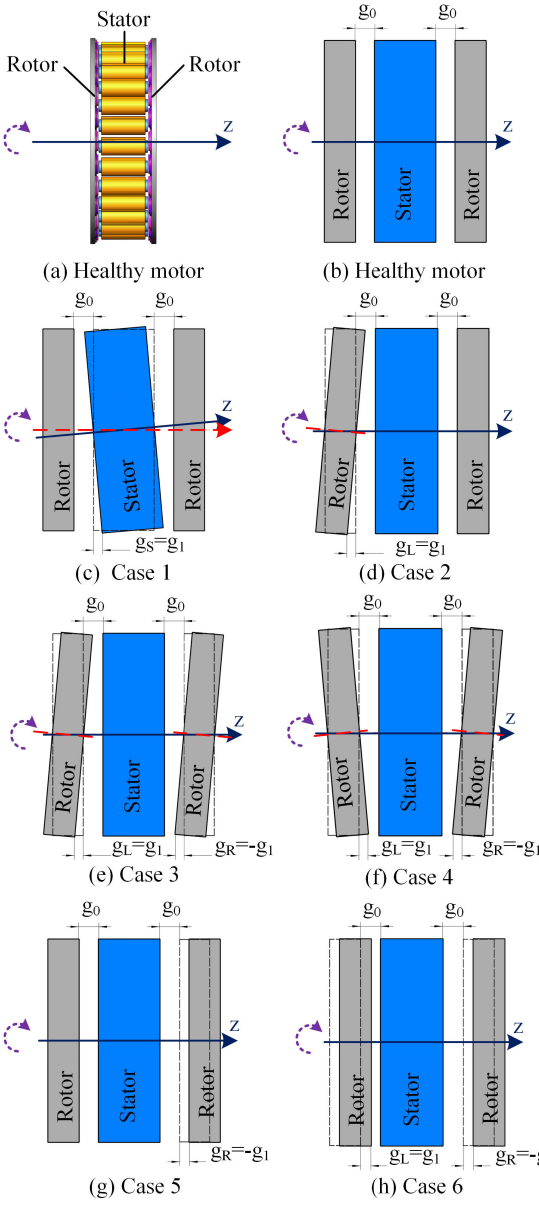

FIGURE 16. Eccentricity and axial offset type. (a) Healthy motor, Diagram of (b) healthy motor, (c) static eccentricity, (d) one-sided rotor dynamic eccentricity, (e) double-sided rotor dynamic eccentricity, (f) double-sided rotor symmetrical dynamic eccentricity, (g) one-sided rotor axial offset, and (h) double-sided rotor axial offset. The *z*-axis represents the stator center. The red dotted line represents the rotor center. The black dotted line represents the position of the stator and rotor of the healthy motor.

be simplified to one-sided rotor axial offset and double-sided rotor offset, as shown in Fig. 16 (g) and (h), respectively.

When the motor is eccentric or axially offset, the air gap length of the motor changes. The static eccentricity coefficient (SEF), the dynamic eccentricity coefficient (DEF), and the axial offset coefficient (AOF) can be expressed as:

$$\mathrm{SEF} = \frac{g_S}{g_0} \times 100\% \tag{8}$$

$$\mathrm{DEF} = \mathrm{AOF} = \frac{g_R}{g_0} \times 100\% \tag{9}$$

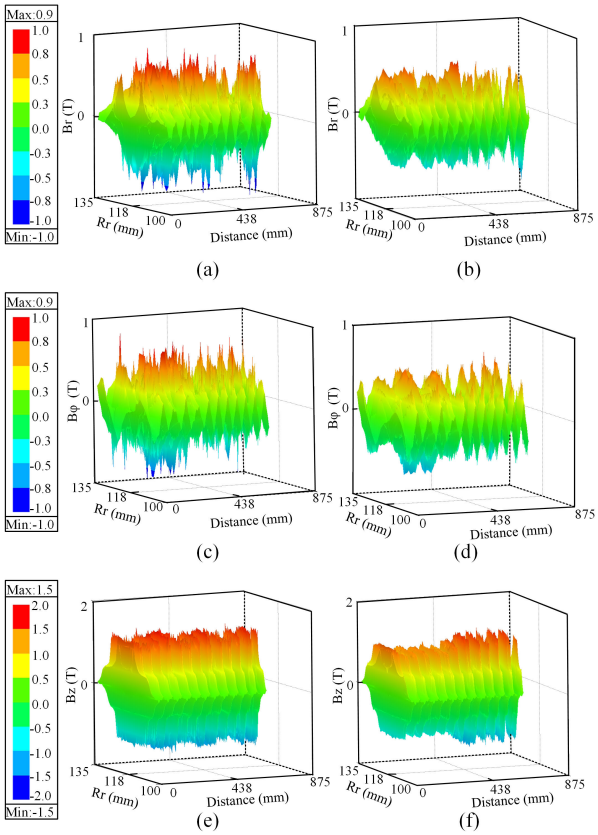

FIGURE 17. Air gap flux density, including the radial-flux density of (a) the healthy condition and (b) the SE condition, the circumferential-flux density of (c) the healthy condition and (d) the SE condition, and the axial-flux density of (e) the healthy condition and (f) the SE condition.

where g_S is the maximum value of the stator position change in the SE condition, g_R is the maximum value of the rotor position change in the condition of DE or AO. The values of SEF, DEF, and AOF in this paper range from 0 to 40%.

Taking the motor in the healthy condition and the SE condition as an example, the variation in the air gap flux density in the radial, circumferential, and axial direction is as shown in Fig. 17. A SEF=40% is selected in the SE condition because it can better show the effect of SE on the air gap flux density. It can be seen that the change in the air gap flux density in the radial and axial direction is not obvious, but there is a significant change in the axial direction. Fig. 18 shows the axial-flux density distribution of the air gap in the healthy and SE condition. When the rotor is not eccentric, the air gap magnetic density distribution is relatively uniform. In the case of SE, the air gap flux density is the largest when the air gap length is the smallest, and the air gap flux density is the smallest when the air gap length is the largest. This is mainly due to the change in the air gap length caused by the eccentricity. When the air gap length is decreased, the magnetic reluctance of the air gap is decreased, and the magnetic potential difference is also decreased, thus the air gap flux density is increased. Conversely, when the air gap length is increased, the magnetic reluctance of the air gap is increased, and the magnetic potential

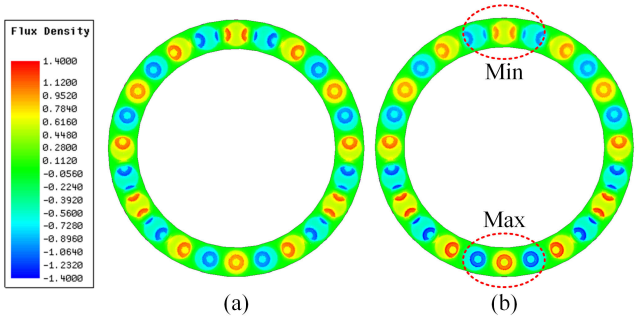

FIGURE 18. Front view of the no-load flux density in the air gap 0.3 mm below the PM. (a) Healthy condition, (b) SE condition with SEF = 40%.

difference is increased, and the air gap flux density is decreased.

The axial force F_z of the single-sided rotor can be obtained by the Maxwell stress tensor (MST) method:

$$F_z = \int_0^{2\pi} \int_{R_i}^{R_o} f_z r dr d\varphi \tag{10}$$

$$f_z = (B_z^2 - B_r^2 - B_\varphi^2)/2\mu_0 \tag{11}$$

where R_o and R_i are the inner and outer diameters of the rotor, respectively, f_z is the axial electromagnetic force density, B_r, B_φ and B_z are the radial, circumferential and axial air gap flux densities, respectively and μ_0 is the permeability of the vacuum.

Due to the open-slot structure of the stator, the axial force in the single-sided rotor of the healthy motor is unevenly distributed along the circumferential direction, as shown in Fig. 19. The axial electromagnetic force wave is generated when the motor is running. To better show the effect of eccentric and axial offset defects on the distribution of electromagnetic force, the values of SEF, DEF and AOF are 40%. In the SE condition, the nonuniformity of the axial force of the rotor is further enhanced. The axial force increases when the air gap flux density is high. Similarly, the axial force at the position with low air gap flux density decreases. In the DE condition, the distribution of the axial force of the rotor is affected by the deflection direction of both rotors. In case 2, the axial force of the deflection side rotor changes obviously. However, the axial force on the nondeflection side did not change significantly. In case 3, the amplitude and distribution of the axial force are similar to those of the SE condition. In case 4, the amplitude and distribution of the axial force of both rotors are the same. In case 5, the axial force decreases when the air gap increases. However, the axial force on the nondeflection side did not change significantly. In case 6, the axial force on both sides changes, and the axial force on the reduced side of the air gap increases, so that the constant axial force on the rotor support also increases. Moreover, the axial offset does not cause additional bending moments in the rotor support.

The axial force on both sides of the stator of the healthy motor is equal, and the direction is inverted. In case 1,

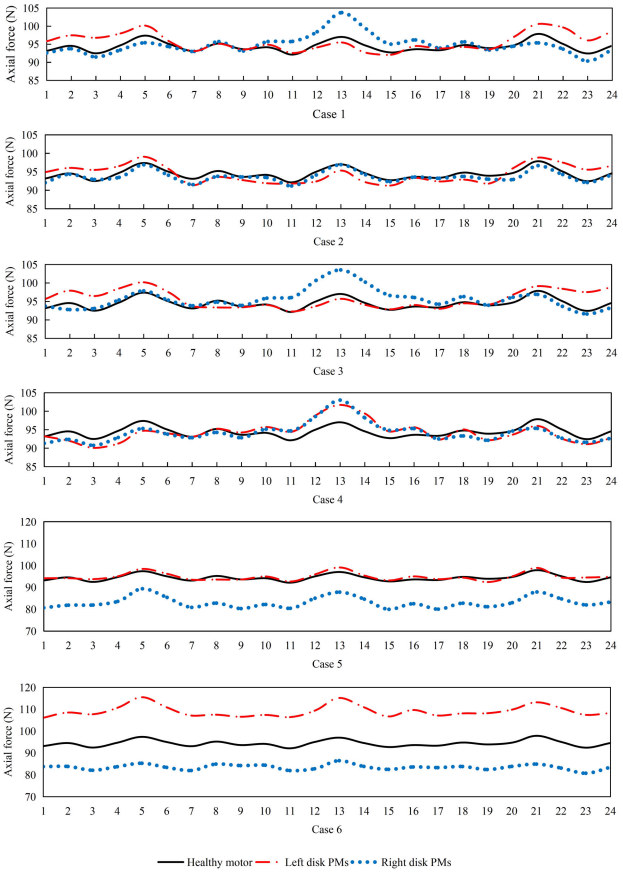

FIGURE 19. The axial force of the rotor disk. The abscissa represents the sequence number of the PMs.

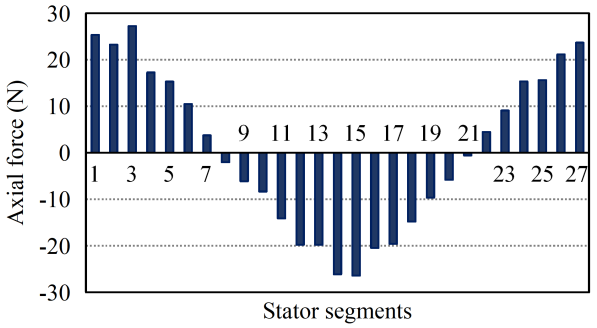

FIGURE 20. The axial force of the stator segments in the SE condition.

the axial force on the stator is still zero, but the axial force on each stator segment is different, as shown in Fig. 20. The stator segments at the extremes of the air gap are subjected to the greatest constant axial force. The constant bending moment of the stator is proportional to the SEF, as shown in Fig. 21. In the DE condition, the axial force on each stator segment changes periodically with the rotation of the rotor. When the rotor rotates, the axial force of the stator segment in three DE conditions is shown in Fig. 22. In case 3, the amplitude of the axial force in the stator segment is the largest. In case 4, the axial force of the stator segment is

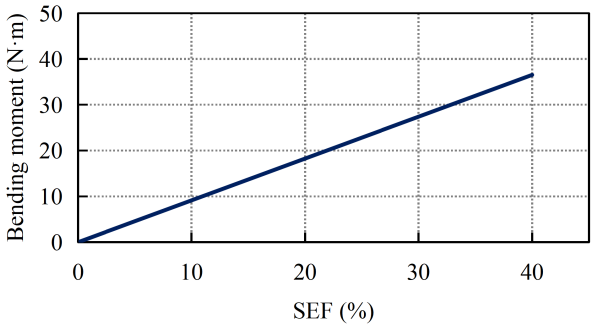

FIGURE 21. The bending moment of the stator in the SE condition.

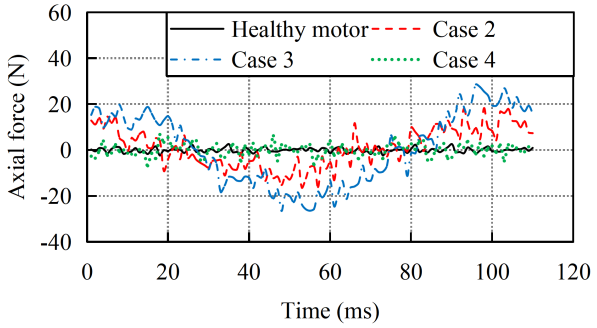

FIGURE 22. The axial force of the stator segment in the DE condition.

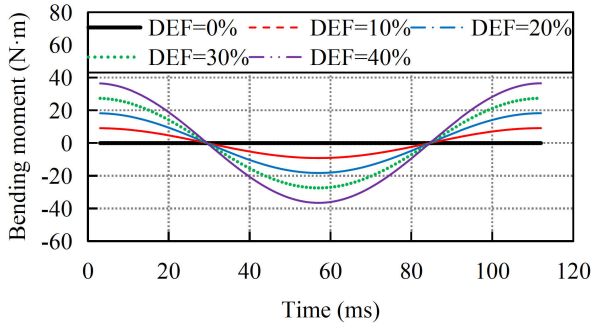

FIGURE 23. The bending moment of the stator in the DE condition.

similar to that of a healthy motor. The bending moment of the stator is caused by the asymmetry of the rotors on both sides. In addition, the direction of the bending moment changes periodically with the rotation of the rotor, and its frequency is the same as that of the rotor. The bending moment causes the bearing to be subjected to alternating reaction forces, which reduces the bearing life, and the bending moment has a tendency to increase the DEF further. The variation of the bending moment of the stator in any direction with different DEFs is shown in Fig. 23. When the rotor is axially offset, the larger the difference between the two sides of the air gap, the greater the axial force on the stator is. In case 6, the axial force on the stator is 571 N. Moreover, the axial offset does not produce bending moments on the stator.

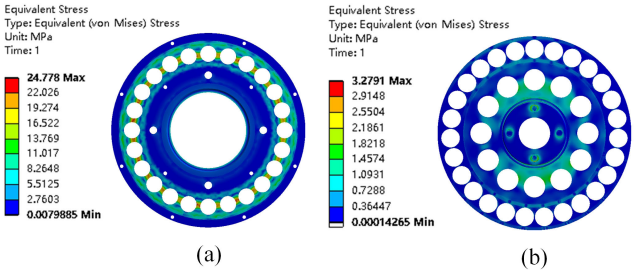

FIGURE 24. Structure analysis of (a) rotor support and (b) stator support.

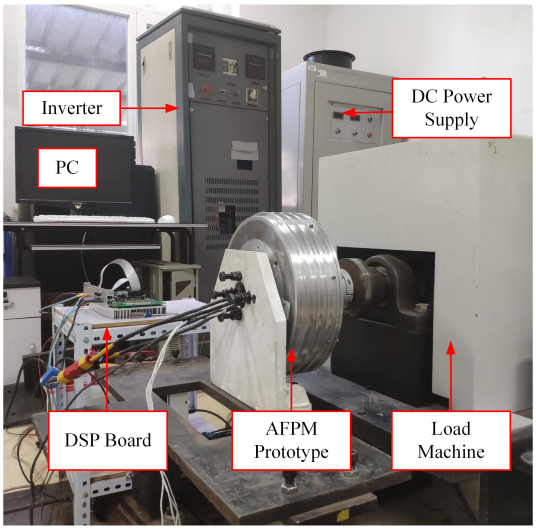

FIGURE 25. Experimental test facility.

From the above analysis, the axial force between the left rotor and the stator in case 6 is the largest. The axial force is applied to the rotor support and the stator support, and the von Mises stress is obtained, as shown in Fig. 24. It was noted that the maximum equivalent stress is much lower than the allowable tensile yield strength of the aluminum alloy (524 MPa). Both the rotor and stator supports are safe enough.

IV. EXPERIMENTAL VERIFICATION

The no-load back EMF, electromagnetic torque, and temperature of the motor are tested in this section. As shown in Fig. 25, the main structure of the experimental bench consists of an axial-flux in-wheel motor, a drive controller, a dynamometer, a DC regulated power supply, an oscilloscope, and a torque instrument. T-type thermocouple sensors are embedded in the stator segment, winding end, and stator support to measure the temperature inside the motor. An infrared thermometer is used to measure the temperature of the rotor back iron and the rotor support. The measured back EMF at 560 r/min is recorded. The results match well with the simulated results, as shown in Fig. 26. The average value of the torque is 24.6 and 23.7 N·m in the FEA and experimental results, respectively. The experimental results achieved approximately 4% less torque than the simulated

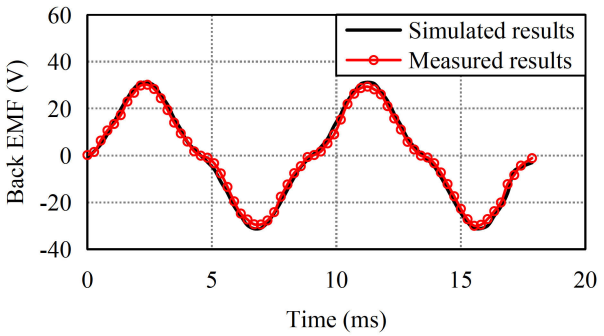

FIGURE 26. Comparison of the back EMF.

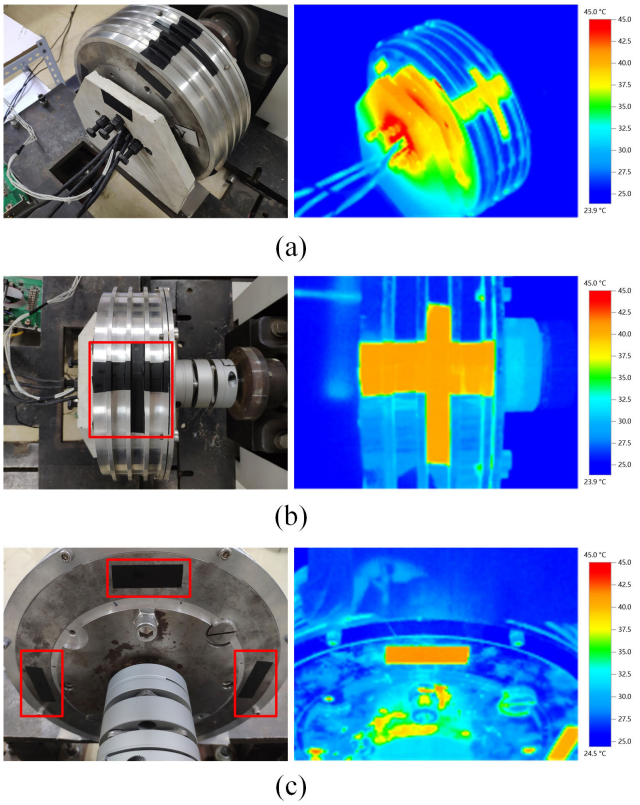

FIGURE 27. Temperature test. (a) Temperature distribution and test points at (b) rotor support and (c) rotor back iron.

results. One of the reasons for the difference is mechanical loss, which is not considered in the simulation.

The temperature of the environment is maintained at 25°C. The motor runs for 60 minutes under rated conditions and 5 minutes under overload conditions. The internal temperature of the motor is read by the PC. Four test points are selected along the circumferential direction on the surface of rotor back iron and rotor support, as shown in Fig. 27(a). Fig. 27(b) shows the test points of the rotor support and Fig. 27(c) shows the test points of the rotor back iron. The average temperature of the four test points is taken as the test result. The test results are shown in Table 4. The experimental values are mainly in agreement with the simulated values, verifying the correctness of the equivalent thermal model.

TABLE 4. The temperature of each component.

Components	Rated condition (560 r/min, 1.3 kW)		Overload condition (280 r/min, 2 kW)	
	Measured temperature (°C)	Simulated temperature (°C)	Measured temperature (°C)	Simulated temperature (°C)
Stator core	93.8	88.2	116.6	111.8
Rotor core	65.6	67.9	91.7	96.8
Winding	101.5	99.5	122.4	120.8
Stator support	79.1	75.1	114.8	104.8
Rotor support	43.8	45.1	76.9	74.7

V. CONCLUSION

In this paper, an axial-flux in-wheel motor with wound AMM stator segments and round PMs is proposed. A multiphysics design, including electromagnetic, thermal, and mechanical aspects, has been introduced, and the multiphysics analysis of the motor is carried out. The electromagnetic characteristic of the designed motor is analyzed by using the 3-D FEM model. The loss of each component is calculated, the eddy-current density of PMs with different shapes is compared, and the round PMs which are easily machined are adopted. The equivalent thermal model of the wound AMM segments and the windings is established, and the temperature distribution of each component of the motor is obtained. The mechanical deviation of the motor is decomposed and the air gap flux density is found to be distorted when the motor is eccentric or axially offset. The mechanical behavior of the rotor and stator teeth under different eccentric and axial offset conditions is analyzed, and the strength of the stator support and rotor support is evaluated. The fabricated motor is tested, and the test results are found to match those of the multiphysics analysis. Hence, the proposed axial-flux in-wheel motor with an AMM stator can be a simple, efficient, and reliable option for EVs.

REFERENCES

[1] J. Zhao, Q. Han, Y. Dai, and M. Hua, "Study on the electromagnetic design and analysis of axial flux permanent magnet synchronous motors for electric vehicles," *Energies*, vol. 12, no. 18, p. 3451, Sep. 2019.

[2] X. Sun, K. Diao, Z. Yang, G. Lei, Y. Guo, and J. Zhu, "Direct torque control based on a fast modeling method for a segmented-rotor switched reluctance motor in HEV application," *IEEE J. Emerg. Sel. Topics Power Electron.*, to be published.

[3] L. Guo, P. Ge, and D. Sun, "Torque distribution algorithm for stability control of electric vehicle driven by four in-wheel motors under emergency conditions," *IEEE Access*, vol. 7, pp. 104737–104748, 2019.

[4] K. Sone, M. Takemoto, S. Ogasawara, K. Takezaki, and H. Akiyama, "A ferrite PM in-wheel motor without rare earth materials for electric city commuters," *IEEE Trans. Magn.*, vol. 48, no. 11, pp. 2961–2964, Nov. 2012.

[5] M. Lehr, K. Reis, and A. Binder, "Comparison of axial flux and radial flux machines for the use in wheel hub drives," *Elektrotechnik Informationstechnik*, vol. 132, no. 1, pp. 25–32, Feb. 2015.

[6] W. Deng and S. Zuo, "Analytical modeling of the electromagnetic vibration and noise for an external-rotor axial-flux in-wheel motor," *IEEE Trans. Ind. Electron.*, vol. 65, no. 3, pp. 1991–2000, Mar. 2018.

[7] T. Takahashi, M. Takemoto, S. Ogasawara, W. Hino, and K. Takezaki, "Size and weight reduction of an in-wheel axial-gap motor using ferrite permanent magnets for electric commuter cars," *IEEE Trans. Ind. Appl.*, vol. 53, no. 4, pp. 3927–3935, Jul. 2017.

[8] W. Deng, S. Zuo, F. Lin, and S. Wu, "Influence of pole and slot combinations on vibration and noise in external rotor axial flux in-wheel motors," *IET Electr. Power Appl.*, vol. 11, no. 4, pp. 586–594, Apr. 2017.

[9] B. Zhang, T. Seidler, R. Dierken, and M. Doppelbauer, "Development of a yokeless and segmented armature axial flux machine," *IEEE Trans. Ind. Electron.*, vol. 63, no. 4, pp. 2062–2071, Apr. 2015.
[10] H. Vansompel, P. Leijnen, and P. Sergeant, "Multiphysics analysis of a stator construction method in yokeless and segmented armature axial flux PM machines," *IEEE Trans. Energy Convers.*, vol. 34, no. 1, pp. 139–146, Mar. 2019.
[11] Z. Wang, R. Masaki, S. Morinaga, Y. Enomoto, H. Itabashi, M. Ito, and S. Tanigawa, "Development of an axial gap motor with amorphous metal cores," *IEEE Trans. Ind. Appl.*, vol. 47, no. 3, pp. 1293–1299, May 2011.
[12] W. Tong, S. Dai, S. Wu, and R. Tang, "Performance comparison between an amorphous metal PMSM and a silicon steel PMSM," *IEEE Trans. Magn.*, vol. 55, no. 6, pp. 1–5, Mar. 2019.
[13] S. Kahourzade, N. Ertugrul, and W. L. Soong, "Loss analysis and efficiency improvement of an axial-flux PM amorphous magnetic material machine," *IEEE Trans. Ind. Electron.*, vol. 65, no. 7, pp. 5376–5383, Jul. 2018.
[14] S. Wu, R. Tang, W. Tong, and X. Han, "Analytical model for predicting vibration due to magnetostriction in axial flux permanent magnet machines with amorphous metal cores," *IEEE Trans. Magn.*, vol. 53, no. 8, pp. 1–8, Aug. 2017.
[15] N. Ertugrul, R. Hasegawa, W. L. Soong, J. Gayler, S. Kloeden, and S. Kahourzade, "A novel tapered rotating electrical machine topology utilizing cut amorphous magnetic material," *IEEE Trans. Magn.*, vol. 51, no. 7, Jul. 2015, Art. no. 2001508.
[16] C. Jensen, F. Profumo, and T. Lipo, "A low-loss permanent-magnet brushless DC motor utilizing tape wound amorphous iron," *IEEE Trans. Ind. Appl.*, vol. 28, no. 3, pp. 646–651, 1992.
[17] Z. Wang, Y. Enomoto, M. Ito, R. Masaki, S. Morinaga, H. Itabashi, and S. Tanigawa, "Development of a permanent magnet motor utilizing amorphous wound cores," *IEEE Trans. Magn.*, vol. 46, no. 2, pp. 570–573, Feb. 2010.
[18] W. Jara, P. Lindh, J. A. Tapia, I. Petrov, A. K. Repo, and J. Pyrhonen, "Rotor eddy current losses reduction in an axial flux permanent magnet machine," *IEEE Trans. Ind. Electron.*, vol. 63, no. 8, pp. 4729–4737, Mar. 2016.
[19] F. Marignetti and V. Colli, "Thermal analysis of an axial flux permanent-magnet synchronous machine," *IEEE Trans. Magn.*, vol. 45, no. 7, pp. 2970–2975, Jul. 2009.
[20] P. Sergeant, H. Vansompel, and L. Dupré, "Influence of stator slot openings on losses and torque in axial flux permanent magnet machines," *Math. Comput. Simul.*, vol. 130, pp. 22–31, Dec. 2016.
[21] J. Li, D.-W. Choi, D.-H. Son, and Y.-H. Cho, "Effects of MMF harmonics on rotor eddy-current losses for inner-rotor fractional slot axial flux permanent magnet synchronous machines," *IEEE Trans. Magn.*, vol. 48, no. 2, pp. 839–842, Feb. 2012.
[22] P. Lindh, I. Petrov, A. Jaatinen-Varri, A. Gronman, M. Martinez-Iturralde, M. Satrustegui, and J. Pyrhonen, "Direct liquid cooling method verified with an axial-flux permanent-magnet traction machine prototype," *IEEE Trans. Ind. Electron.*, vol. 64, no. 8, pp. 6086–6095, Aug. 2017.
[23] Q. Chen, D. Liang, L. Gao, Q. Wang, and Y. Liu, "Hierarchical thermal network analysis of axial-flux permanent-magnet synchronous machine for electric motorcycle," *IET Electric Power Appl.*, vol. 12, no. 6, pp. 859–866, Jul. 2018.
[24] D. H. Lim and S. C. Kim, "Thermal performance of oil spray cooling system for in-wheel motor in electric vehicles," *Appl. Thermal Eng.*, vol. 63, no. 2, pp. 577–587, Feb. 2014.
[25] R. Camilleri, D. A. Howey, and M. D. Mcculloch, "Predicting the temperature and flow distribution in a direct oil-cooled electrical machine with segmented stator," *IEEE Trans. Ind. Electron.*, vol. 63, no. 1, pp. 82–91, Jan. 2016.
[26] Y. C. Chong, E. J. P. Echenique Subiabre, M. A. Mueller, J. Chick, D. A. Staton, and A. S. Mcdonald, "The ventilation effect on stator convective heat transfer of an axial-flux permanent-magnet machine," *IEEE Trans. Ind. Electron.*, vol. 61, no. 8, pp. 4392–4403, Aug. 2014.
[27] Y. Cao, S. Tao, J. Cai, L. Yu, H. Jia, and T. Zhang, "Magnetic field analytical solution and electromagnetic force calculation of coreless stator axial-flux permanent-magnet machines," *Int. J. Appl. Electrom. Mech.*, vol. 54, no. 1, pp. 93–105, Apr. 2017.
[28] J. De Bisschop, P. Sergeant, A. Hemeida, H. Vansompel, and L. Dupre, "Analytical model for combined study of magnet demagnetization and eccentricity defects in axial flux permanent magnet synchronous machines," *IEEE Trans. Magn.*, vol. 53, no. 9, pp. 1–12, Sep. 2017.
[29] E. Ajily, M. Ardebili, and K. Abbaszadeh, "Magnet defect and rotor eccentricity modeling in axial-flux permanent-magnet machines via 3-D field reconstruction method," *IEEE Trans. Energy Convers.*, vol. 31, no. 2, pp. 486–495, Jun. 2016.
[30] Z. Nasiri-Gheidari and H. Lesani, "New design solution for static eccentricity in single stator–single rotor axial flux induction motors," *IET Electr. Power Appl.*, vol. 7, no. 6, pp. 523–534, Jul. 2013.
[31] F. Marignetti, A. Vahedi, and S. M. Mirimani, "An analytical approach to eccentricity in axial flux permanent magnet synchronous generators for wind turbines," *Electr. Power Compon. Syst.*, vol. 43, nos. 8–10, pp. 1039–1050, Jun. 2015.
[32] S. M. Mirimani, A. Vahedi, F. Marignetti, and R. Di Stefano, "An online method for static eccentricity fault detection in axial flux machines," *IEEE Trans. Ind. Electron.*, vol. 62, no. 3, pp. 1931–1942, Mar. 2015.
[33] S. M. Mirimani, A. Vahedi, F. Marignetti, and E. D. Santis, "Static eccentricity fault detection in single-stator-single-rotor axial-flux permanent-magnet machines," *IEEE Trans. Ind. Appl.*, vol. 48, no. 6, pp. 1838–1845, Oct. 2013.
[34] S. M. Mirimani, A. Vahedi, and F. Marignetti, "Effect of inclined static eccentricity fault in single stator-single rotor axial flux permanent magnet machines," *IEEE Trans. Magn.*, vol. 48, no. 1, pp. 143–149, Jul. 2012.
[35] N. Salim, S. P. Nikam, S. Pal, A. K. Wankhede, and B. G. Fernandes, "Multiphysics analysis of printed circuit board winding for high-speed axial flux permanent magnet motor," *IET Electric Power Appl.*, vol. 13, no. 6, pp. 805–811, Jun. 2019.
[36] J. Li, Y. Lu, Y.-H. Cho, and R. Qu, "Design, analysis, and prototyping of a water-cooled axial-flux permanent-magnet machine for large-power direct-driven applications," *IEEE Trans. Ind. Appl.*, vol. 55, no. 4, pp. 3555–3565, Jul. 2019.
[37] H. Vansompel, A. Rasekh, A. Hemeida, J. Vierendeels, and P. Sergeant, "Coupled electromagnetic and thermal analysis of an axial flux PM machine," *IEEE Trans. Magn.*, vol. 51, no. 11, pp. 1–4, Nov. 2015.
[38] F. Marignetti, V. Delli Colli, and Y. Coia, "Design of axial flux PM synchronous machines through 3-D coupled electromagnetic thermal and fluid-dynamical finite-element analysis," *IEEE Trans. Ind. Electron.*, vol. 55, no. 10, pp. 3591–3601, Oct. 2008.
[39] A. Hemeida, A. Lehikoinen, P. Rasilo, H. Vansompel, A. Belahcen, A. Arkkio, and P. Sergeant, "A simple and efficient quasi-3D magnetic equivalent circuit for surface axial flux permanent magnet synchronous machines," *IEEE Trans. Ind. Electron.*, vol. 66, no. 11, pp. 8318–8333, Nov. 2019.
[40] W. Tong, S. Wang, S. Wu, and R. Tang, "A complete quasi-3-D analytical model of no-load magnetic field of double-sided slotted AFPMMs considering end effect," *IEEE Access*, vol. 6, pp. 59557–59566, 2018.
[41] G. Bertotti, "General properties of power losses in soft ferromagnetic materials," *IEEE Trans. Magn.*, vol. 24, no. 1, pp. 621–630, Jan. 1988.
[42] R. Benlamine, F. Dubas, S.-A. Randi, D. Lhotellier, and C. Espanet, "3-D numerical hybrid method for PM eddy-current losses calculation: Application to axial-flux PMSMs," *IEEE Trans. Magn.*, vol. 51, no. 7, Jul. 2015, Art. no. 8106110.
[43] M. Aydin and M. Gulec, "Reduction of cogging torque in double-rotor axial-flux permanent-magnet disk motors: A review of cost-effective magnet-skewing techniques with experimental verification," *IEEE Trans. Ind. Electron.*, vol. 61, no. 9, pp. 5025–5034, Sep. 2014.

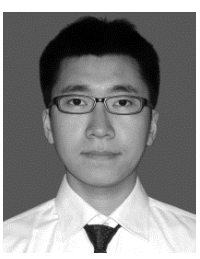

TAO LI was born in Datong, Shanxi, China, in 1989. He received the B.S. and M.S. degrees from the College of Mechatronics Engineering, North University of China, Taiyuan, China, in 2014. He is currently pursuing the Ph.D. degree with the School of Mechanical Engineering, Beijing Institute of Technology, Beijing, China. His research interests include permanent magnet synchronous motor design and analysis, solenoid valve design and analysis, and piezoelectric mechanism design and analysis.

YOUTONG ZHANG was born in Jilin City, Jilin, China, in 1965. He received the B.S. and M.S. degrees in engine engineering from Jilin University, Changchun, in 1990, and the Ph.D. degree from the College of Mechatronics Engineering, Beijing Institute of Technology, Beijing, China, in 1995. He is currently a Professor with the College of Mechatronics Engineering, Beijing Institute of Technology. He is also the Director of the Laboratory of Low Emission Vehicle, Beijing Institute of Technology. He authored two books and has more than 60 articles. His research interests include engine electronic control and new energy vehicle.

YUXIU LIANG was born in Baoding, Hebei, China, in 1988. She received the B.S. and M.S. degrees from the School of Mechanical Engineering, North University of China, Taiyuan, China, in 2015. She is currently pursuing the Ph.D. degree with the School of Mechanical Engineering, Beijing Institute of Technology, Beijing, China. Her research interests include multiphase flow in solenoid valve of fuel supply systems in engines and multiphysics analysis of the solenoid valve.

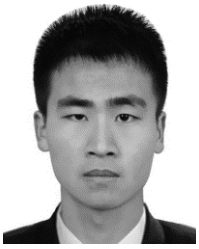

QIANG AI was born in Tangshan, Hebei, China, in 1992. He received the B.S. degree from the School of Mechanical Engineering, Beijing Institute of Technology, Beijing, China, in 2017, where he is currently pursuing the Ph.D. degree with the School of Mechanical Engineering. His research interests include permanent magnet synchronous motor and multiobjective optimization algorithm.

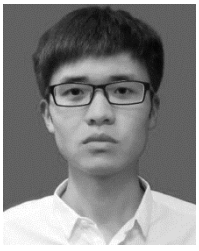

HAISHI DOU was born in Luan, Anhui, China, in 1994. He received the B.S. degree from the Anhui Institute of Information Technology, China, in 2017, and the M.S. degree in mechanical engineering from the Anhui University of Science and Technology, China, in 2019. He is currently pursuing the Ph.D. degree with the School of Mechanical Engineering, Beijing Institute of Technology, Beijing, China. His research interest includes the motor control systems.